Article

Multi-Criteria Analysis of Operating Line Selection for Hydrogen Engine PHEVs

Oleksandr Osetrov * and Rainer Haas

Posted Date: 30 April 2026

doi: 10.20944/preprints202604.2108.v1

Keywords: hydrogen engine; plug-in hybrid electric vehicle; engine operating line; rule-based energy management strategy; Analytic Hierarchy Process; Technique for Order Preference by Similarity to Ideal Solution

 doi:10.20944/preprints202604.2108.v1

Article

Multi-Criteria Analysis of Operating Line Selection for Hydrogen Engine PHEVs

Oleksandr Osetrov * and Rainer Haas

Faculty of Automotive Systems and Production, TH Köln - University of Applied Sciences, 50679 Köln, Germany; rainer.haas@th-koeln.de
* Correspondence: oleksandr.osetrov@th-koeln.de

Abstract

The transition to a hydrogen-based energy economy emphasizes the potential of hydrogen as a fuel for plug-in hybrid electric vehicles (PHEVs). The performance of a hydrogen engine within a PHEV depends on the choice of its operating modes, which influence both efficiency and emissions. This study proposes a method for developing engine operating lines (EOLs) on engine maps based on minimizing nitrogen oxide (NOx) emissions while considering constraints on maximum engine power. A total of 15 EOLs are proposed for configurations with both constant and variable maximum engine power. Using mathematical modeling of PHEV operation under the Worldwide Harmonized Light Vehicles Test Cycle (WLTC), the impact of EOL selection on engine characteristics, as well as on battery and generator parameters, is analyzed. For a comprehensive evaluation of EOL effectiveness, five criteria are introduced, considering fuel energy consumption, NOx emissions, wear, mechanical fatigue, and noise, vibration, and harshness (NVH). The Analytic Hierarchy Process (AHP) and the Technique for Order Preference by Similarity to Ideal Solution (TOPSIS) are applied to determine the weighting factors of the criteria and to rank the proposed EOLs, thereby identifying the most efficient configurations. The results show that, for the base hydrogen engine configuration, selecting appropriate operating modes alone enables NOx emissions to be reduced significantly below Euro 6 limits, without any hardware modifications or exhaust aftertreatment.

Keywords: hydrogen engine; plug-in hybrid electric vehicle; engine operating line; rule-based energy management strategy; Analytic Hierarchy Process; Technique for Order Preference by Similarity to Ideal Solution

1. Introduction

The development of "green" energy involves not only increasing electricity generation from renewable sources but also the large-scale production of hydrogen via electrolysis for energy storage, transportation, and subsequent conversion [1–3]. According to European Union plans, by 2030, electrolyzers with a total capacity of 40 GW, powered by renewable energy, are expected to be installed, enabling the annual production of approximately 10 million tons of "green" hydrogen [1]. At the same time, the expansion of hydrogen infrastructure and large-scale imports are also planned [2,3].

In parallel with the growth of hydrogen production and consumption, environmental requirements for vehicle powertrains using conventional fuels are becoming increasingly stringent. Regulation (EU) 2019/631 sets a target of zero CO_2 emissions by 2035, which effectively implies a ban on the use of gasoline and diesel fuels [4]. Moreover, Regulation (EU) 2023/851 [5] explicitly prohibits the sale of new vehicles equipped with internal combustion engines (hereinafter referred to as "engines") powered by gasoline or diesel starting in 2035.

 doi:10.20944/preprints202604.2108.v1

These legislative measures stimulate both the electrification of vehicles and the development of hydrogen-based powertrain technologies. In this context, the application of series plug-in hybrid electric vehicles (PHEVs) equipped with hydrogen engines appears particularly promising. In PHEVs, there is no direct mechanical connection between the engine and the wheels, which allows for highly efficient optimization of engine operating modes [6,7].

Furthermore, the fuel properties of hydrogen—such as its high gravimetric lower heating value, absence of carbon, wide flammability limits, and high combustion speed in stoichiometric mixtures with air—enable engine performance comparable to that of modern diesel engines, while maintaining nitrogen oxides (NOx) emissions at Euro 6 levels without the need for exhaust aftertreatment systems [8–11]. Examples of hydrogen internal combustion engines already exist in series production [12], while several others are currently at the pre-production development stage [13,14].

The efficiency of the engine, generator, battery, and electric motor (hereinafter referred to as the "motor") in a PHEV depends on the energy management system (EMS), which governs the interaction between power sources (the so-called power split) to deliver the required traction. Currently, rule-based (RB) EMS and optimization-based (OB) EMS are widely used [15,16].

Rule-based EMS are primarily heuristic methods that rely on a set of predefined rules, generating control commands based on thresholds of key variables [6,15,17,18]. In contrast, optimization-based EMS determine the power split by minimizing an objective (or cost) function subject to various constraints [6,19–23].

When RB EMS are applied to PHEVs equipped with gasoline or diesel engines, the operating modes are typically located along engine operating lines (EOLs) passing through regions of maximum brake thermal efficiency (BTE) on the engine map [18,20,24]. In OB EMS, the primary optimization criterion for selecting engine modes is usually the equivalent fuel consumption, which accounts for both the direct fuel consumption of the engine and the battery energy consumption converted into equivalent fuel units [7,19,21,25]. Less commonly, additional constraints or criteria—such as the number of engine start–stop events [6] or noise limitations [17]—are incorporated into the objective function.

It should be noted that nitrogen oxides emissions are a key parameter for hydrogen engines. These emissions can be reduced to near-zero levels through the use of lean air–fuel mixtures and other measures [8–11]. Consequently, NOx emissions are often given primary importance in the optimization of hydrogen engines [12–14,26,27]. However, in hybrid electric vehicles (HEVs) equipped with hydrogen engines, approaches similar to those used for conventional engines are frequently applied when selecting optimization criteria [28–32].

In this context, the studies [33,34] deserve particular attention, as they include NOx emissions alongside fuel consumption as optimization criteria. Machacek et al. [33] investigated the application of a hydrogen engine in series, parallel, and power-split hybrid electric vehicle (HEV) configurations. The cost function in their OB EMS accounted for both equivalent fuel consumption and NOx emissions. Based on Pareto front analysis using dynamic programming, EMS calibrations were obtained for various driving cycles.

The results indicate that when NOx minimization is prioritized over fuel consumption, the engine operating points for a series HEV lie along an iso-NOx line on the engine map, above which NOx emissions increase sharply. In this case, the maximum torque is approximately 1.4 times lower than the corresponding value obtained when minimizing fuel consumption. However, the study does not address how this affects engine start–stop frequency, fatigue, component wear, battery aging, or other powertrain reliability-related parameters.

Bloch et al. [34] presented experimental results for a hydrogen engine operating in a PHEV. In this study, the main optimization parameters in the cost function are BTE and NOx, with weights varying from 0 to 1 in increments of 0.2. For each combination of weights, engine operating lines (EOLs) are defined on the BTE map. Notably, for several EOLs with NOx weights ranging from 0 to 0.8, the maximum power is approximately 60 kW, whereas for an NOx weight of 1, the maximum power decreases significantly to about 44 kW. The reasons for this behavior, as well as specific aspects

 doi:10.20944/preprints202604.2108.v1

of the optimization procedure, are not discussed. It is also shown that increasing the NOx weight relative to BTE leads to a substantial reduction in engine torque, accompanied by an increase in engine speed. However, the impact of this shift on other engine and overall powertrain parameters is not addressed.

It can be concluded that determining the operating conditions of a hydrogen engine in a PHEV, based on a trade-off between fuel efficiency and NOx emissions, remains a relevant research problem. At the same time, methodologies for developing EOLs for this purpose—particularly in the context of RB EMS—are insufficiently represented in the literature.

Available studies indicate that prioritizing NOx minimization leads to significant changes in reliability-related engine parameters compared to strategies focused on minimizing fuel consumption. This highlights the need to account for such parameters.

The objective of this study is to determine the most efficient operating modes for a hydrogen engine in a PHEV, balancing fuel efficiency, NOx emissions, and their impact on reliability-related parameters.

2. Materials and Methods

2.1. Object of Study

This study is based on the results reported in [34–37], concerning a hydrogen-fueled 1.0 L Ford EcoBoost engine operating in a PHEV. The powertrain architecture of the vehicle is shown in Figure 1, and the main PHEV parameters are summarized in Table 1.

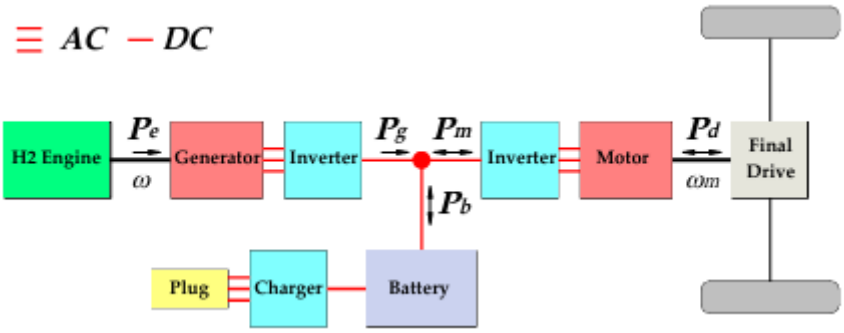

Figure 1. Powertrain layout of the series PHEV: *Pe*, *Pg*, *Pm*, and *Pb* denote the power of the engine, generator, motor, and battery, respectively; ω and ω_m represent the rotational speeds of the engine and motor; AC—alternating current; DC—direct current.

It should be noted that the engine and generator are directly coupled, while the motor drives the wheels through a fixed gear ratio of 13.18. This type of PHEV architecture is relatively uncommon and requires the electric motor to operate at comparatively high rotational speeds (on the order of 13,000 rpm). In the present study, the baseline PHEV parameters from [34] are adopted without modification.

Table 1. PHEV powertrain parameters [34].

Component	Parameter	Value
Battery	Capacity	36.6 Ah
Generator	Power	60 kW
Motor	Power	90 kW
Engine	Displacement	1.0 L
	Cylinders	3, in-line
	Bore × Stroke	71.9 mm × 82 mm

 doi:10.20944/preprints202604.2108.v1

	Rated power	60 kW at 5000 rpm
	Features	Direct injection, variable geometry turbine
Transmission	Engine-to-generator ratio	1
	Motor-to-wheels ratio	13.18
	Efficiency	96 %

2.2. Mathematical Models

2.1.1. Energy Management Strategy

In this study, a so-called backward-type powertrain model is employed, in which the required parameters of the PHEV components (speeds, power, efficiencies, torques, voltages, etc.) are determined sequentially at each time step based on the prescribed vehicle driving conditions.

The vehicle is assumed to operate on a flat road under the conditions of the Worldwide Harmonized Light Vehicles Test Cycle (WLTC). The input data for the simulation consist of the vehicle speed profile as a function of time, along with the vehicle mass and other design parameters.

Figure 2 illustrates simplified block diagrams of the power flow control strategies in the powertrain. The following PHEV operating modes can be distinguished: electric drive (battery supplies power to the wheels), regenerative braking (battery charging), combined drive (engine and battery), and engine-driven operation with simultaneous battery charging.

During the simulation, the motor shaft power P_d, angular velocity ω_d, and the corresponding torque T_d are determined as:

$$T_d = \frac{P_d}{\omega_d} . \quad (1)$$

Based on the obtained values of T_d and n_d, the combined efficiency of the motor and inverter η_{MI} is determined from efficiency maps (see Section 2.2.2), and the battery charging/discharging power is calculated as:

$$P_m = \begin{cases} \frac{P_d}{\eta_{MI}}, & P_d \geq 0 \\ P_d \eta_{MI} \eta_{rec}, & P_d < 0 \end{cases}, \quad (2)$$

where η_{rec} is the battery recuperation efficiency.

During braking, the maximum recuperation power is limited to a predefined value P_{r_max}:

$$P_m = max(P_m, -P_{r\_max}). \quad (3)$$

 doi:10.20944/preprints202604.2108.v1

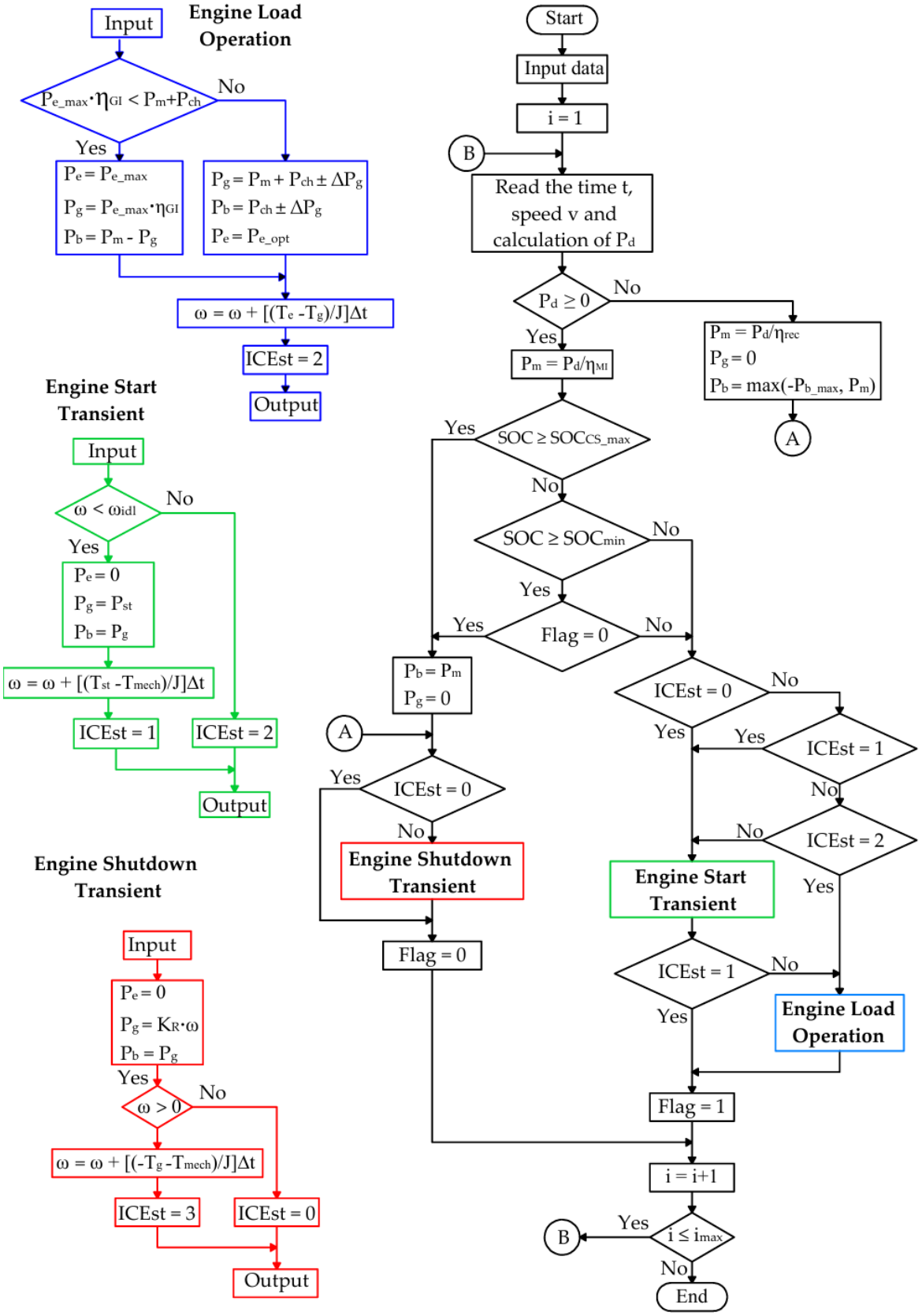

Figure 2. Simplified block diagrams of power flow control in the powertrain. .

According to the adopted rule-based strategy, a hysteresis-based engine control algorithm is applied, based on the battery state of charge (SOC). When the SOC is between its maximum SOC_{max}

 doi:10.20944/preprints202604.2108.v1

and minimum SOC_{min} values, the vehicle operates in pure electric mode, and the required traction power is supplied entirely by the battery:

$$P_b = P_m. \tag{4}$$

When the SOC reaches SOC_{min}, the engine is activated, and the vehicle switches to charge-sustaining (CS) mode. In this mode, the SOC is maintained within the range from its minimun SOC_{min} to the maximum specified in CS mode, SOC_{CS_max}. When the SOC reaches SOC_{CS_max}, the engine is switched off and remains off until the SOC drops again to SOC_{min}, at which point the cycle repeats.

The hysteresis behavior of engine activation and deactivation is implemented using a control flag variable (Flag). When Flag = 0, the engine is off, and propulsion in CS mode is provided by the battery; when Flag = 1, propulsion is provided by the engine.

When the engine is activated, the electrical power generated by the generator is calculated as:

$$P_g = \begin{cases} P_m + P_{ch}, P_m + P_{ch} \leq P_{g\_max} \\ P_{g\_max}, P_m + P_{ch} > P_{g\_max} \end{cases}, \tag{5}$$

where P_{ch} is the battery charging power and P_{g_max} is the maximum generator power.

The maximum generator power is determined by the maximum engine power:

$$P_{g\_max} = P_{e\_max}\eta_{GI}, \tag{6}$$

where P_{e_max} is the maximum engine power and η_{GI} is the combined efficiency of the generator and inverter.

If $P_m + P_{ch} > P_{g\_max}$, the battery charging power is reduced accordingly. If $P_m > P_{g\_max}$, the battery supplies the deficit power required for traction:

$$P_b = P_m - P_{g\_max}. \tag{7}$$

The calculated generator power determines the required engine power. Based on the predefined EOL and the required engine power at a given operating point, the target engine speed n_{tar}, brake mean effective pressure (BMEP), and torque T_{e_tar} are determined.

A distinctive feature of the model is the consideration of engine and generator inertia during transient operation under the WLTC cycle. The actual engine torque T_e and speed n lie on one of the predefined EOLs and, in general, differ from the target values T_{e_tar} and n_{tar}. The transition to the target operating point is primarily controlled by adjusting the generator torque using proportional–derivative control. The overall power balance of the PHEV is maintained through energy exchange with the battery.

The engine control depends on its state in the previous time step. The mathematical model defines four engine states, identified by the variable ICE_{st}: 0 – engine off, 1 – engine acceleration from activation to idle speed (idle speed is defined here as the speed at which the engine can accept load), 2 – loaded engine operation, 3 – engine deceleration without load from deactivation to standstill.

In state 1, the engine load is disconnected, and the indicated power is used to overcome mechanical losses P_{mech} and the inertia of rotating components of the engine and generator with total inertia J. Once the idle angular velocity ω_{idl} is reached, the engine torque is set to T_{e_opt}, corresponding to the selected EOL (state 2). The corresponding engine power is denoted as P_{e_opt} in Figure 2.

The generator power P_g is regulated based on the required power for the current WLTC operating point $P_{g\_tar} = P_m + P_{ch}$, the engine acceleration dynamics toward the target angular velocity ω_{targ}, and the velocity deviation $\Delta\omega$.

If the engine operates during regenerative braking or when the SOC exceeds SOC_{CS_max}, it is deactivated (state 3). In this case, the engine speed decreases, and the operating mode is governed by the balance of inertia J, mechanical resistance torque T_{mech}, and the generator torque T_g, which can be used to control engine deceleration.

 doi:10.20944/preprints202604.2108.v1

2.2.2. Mathematical Model of the Hydrogen Engine

The engine performance characteristics are determined using maps of brake thermal efficiency and specific nitrogen oxide emissions (Figure 3). The BTE map is adopted from [34]. In [34], NOx emissions are presented as a ratio between the hydrogen and gasoline engine variants, which makes their direct application in the present study impractical. Therefore, a dedicated mathematical model of NOx formation across the entire engine operating range has been developed.

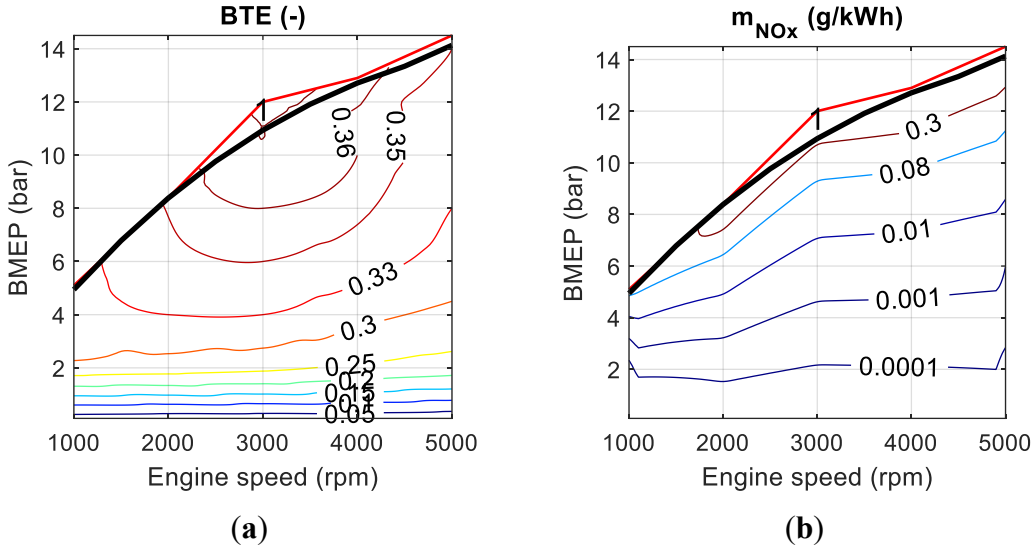

Figure 3. Maps of brake thermal efficiency based on [34] (a) and specific NOx emissions obtained from simulation for the hydrogen engine (b). 1 – engine operating line.

For this purpose, a mathematical model of the hydrogen engine cycle, developed by the authors and described in detail in [38–40], is utilized. The calculated NOx results show good agreement with data reported for turbocharged hydrogen engines with variable mixture composition in [32,35,41], both in terms of absolute values and in terms of their variation as a function of BMEP and engine speed.

The engine operating points in a PHEV are located along one of the EOLs on the maps. Figure 3 shows EOL 1, which passes through the region of maximum BTE. In this study, a total of 15 different EOLs are analyzed, as described in Section 3.1.

During the simulation, the engine brake mean effective pressure and speed n are determined. Subsequently, the BTE and specific NOx emissions m_{NOx} are obtained by interpolating the map data according to the selected operating strategy.

The hydrogen mass flow rate at each operating point is calculated as:

$$\frac{\Delta m_{H_2}}{\Delta t} = \frac{P_e}{BTE \cdot Q_{H_2}}, \tag{8}$$

where Δt is the time step and Q_{H_2} is the lower heating value of hydrogen.

The total hydrogen consumption over the test cycle is given by:

$$m_{H_2\_tot} = \sum_{t=0}^{t_{end}} \frac{\Delta m_{H_2}}{\Delta t} \Delta t, \tag{9}$$

where t_{end} is the end time of the WLTC cycle (t_{end} = 1800 s).

The specific fuel energy consumption per kilometer is calculated as:

$$E_{H_2\_km} = \frac{m_{H_2\_tot} Q_{H_2}}{S}, \tag{10}$$

where S is the total distance traveled.

The instantaneous NOx mass flow rate is defined as:

 doi:10.20944/preprints202604.2108.v1

$$\frac{\Delta m_{NOx}}{\Delta t} = \frac{m_{NOx}}{BTE \cdot Q_{H_2}}. \quad (11)$$

The total NOx emissions over the cycle are calculated as:

$$m_{NOx\_tot} = \sum_{t=0}^{t_{end}} \frac{\Delta m_{NOx}}{\Delta t} \Delta t, \quad (12)$$

and the NOx emissions per kilometer are given by:

$$m_{NOx\_km} = \frac{m_{NOx\_tot}}{s}. \quad (13)$$

The integrated indicators of fuel efficiency and engine emissions are used for the multi-criteria evaluation of the effectiveness of the selected EOLs (see Section 2.3).

2.2.3. Mathematical Models of the Motor and Generator

Since the specifications of the motor and generator are not provided in [34], the following approach is adopted in this study. The efficiency characteristics of the electric machines are determined based on a combined efficiency map of the motor and inverter from [42].

The map is converted into normalized torque coordinates and then linearly scaled according to the specified maximum torque (Figure 4). Map data are subsequently interpolated as a function of the torque and speed, calculated using the backward-type model under WLTC operating conditions.

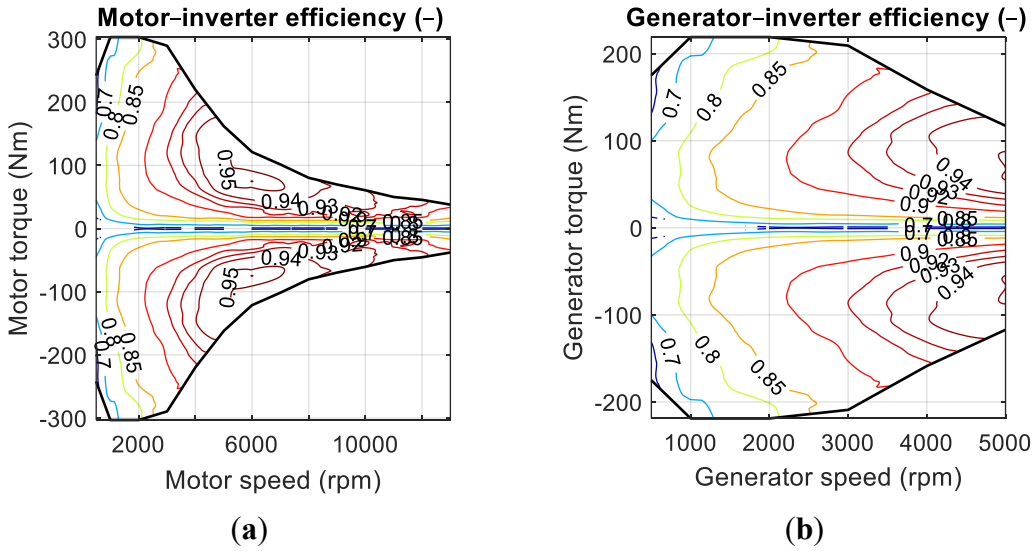

Figure 4. Combined efficiency maps of the motor and inverter (a) and of the generator and inverter (b).

2.2.4. Mathematical Model of the Battery

The battery is modeled using an equivalent circuit consisting of a voltage source and an internal resistance, both dependent on the state of charge (Figure 5) [43,44]. Temperature effects are neglected in the present model. An identical dependence of the internal resistance on SOC is assumed for both charging and discharging conditions (Figure 5b).

 doi:10.20944/preprints202604.2108.v1

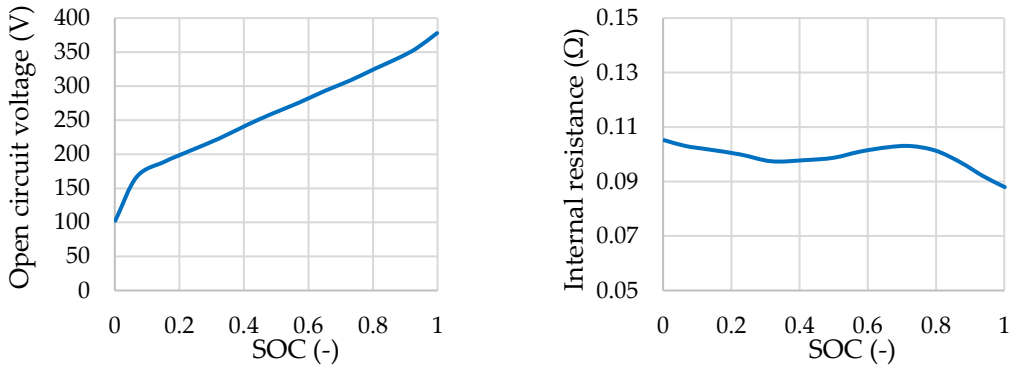

(**a**) (**b**)

Figure 5. Open-circuit voltage (a) and internal resistance of the battery [43,44].

The relationship between battery power, open-circuit voltage, and internal resistance is given by:

$$P_b = V_{oc} I_b - I_b^2 R_{int}, \tag{14}$$

where V_{oc} is the open-circuit voltage, I_b is the battery current, and R_{int} is the internal resistance.

From Equation (14), the battery current can be calculated as:

$$I_b = -\frac{V_{oc} - \sqrt{V_{oc}^2 - 4P_b R_{int}}}{2R_{int}}, \tag{15}$$

The state of charge is updated according to:

$$SOC_{t+\Delta t} = SOC_t + \frac{-I_b \eta_b(I_b) \cdot \Delta t}{C_b}, \tag{16}$$

where Δt is the time step, C_b is the battery capacity, and η_b is the coulombic efficiency (assumed to be 0.9 during charging and 1 during discharging).

The mathematical models presented in Section 2.2 are implemented in the MATLAB R2025a environment.

2.3. Optimization Methods

In this study, 15 EOLs were evaluated using five performance criteria (see Section 3.3). To determine the weights of the selected criteria C_1 – C_5, the Analytic Hierarchy Process (AHP) was employed—a widely used method in engineering for multi-criteria decision-making [45–49].

AHP is based on pairwise comparisons of criteria using the Saaty scale (Table 2) [50], resulting in a comparison matrix:

$$A = [a_{ij}], \tag{17}$$

where a_{ij} represents the relative importance of criterion i over criterion j, chosen according to Table 2. The priority weight vector w is obtained from:

$$Aw = \lambda w, \tag{18}$$

where λ is an eigenvalue of the matrix A, and w is the eigenvector.

The normalized weights are calculated as:

$$w_i = \frac{v_i}{\sum_{k=1}^{n} v_k}, \; i=1,\ldots, n, \tag{19}$$

where v_i is the component of the eigenvector corresponding to criterion C_i, the denominator represents the sum of all components, and n is the number of criteria ($n = 5$).

 doi:10.20944/preprints202604.2108.v1

The consistency of matrix A is verified using the Consistency Ratio (CR), which must satisfy CR ≤ 0.1.

Table 2. Saaty's fundamental pairwise comparison scale [50].

Intensity	Importance of One Over Another	Explanation
1	Equal importance	Two activities contribute equally to the objective
3	Moderate importance	Experience or judgement slightly favors one criterion over another
5	Essential or strong importance	Experience or judgement strongly favors one criterion over another
7	Very strong importance	An activity is strongly favored, and its dominance demonstrated in practice
9	Extreme importance	The evidence favoring one activity over another is of the highest possible
2, 4, 6, 8	Intermediate values	When compromise is needed

To rank the EOL, the Technique for Order Preference by Similarity to Ideal Solution (TOPSIS) method is employed. This method, developed by Hwang and Yoon [51], is widely applied in the multi-criteria optimization of technical systems [46–48,52–54].

The advantages of the TOPSIS method include its relative simplicity and its ability to evaluate multiple criteria simultaneously. Moreover, it enables a clear comparison of alternatives by measuring their distances from the ideal and negative ideal solutions, thereby providing a straightforward ranking of alternatives from best to worst.

In this method, the decision matrix is first constructed:

$$A_d = [x_{ij}], \tag{20}$$

where x_{ij} is the value of criterion j for alternative i, m is the number of alternatives (m = 8), and n is the number of criteria.

The normalized matrix is obtained as:

$$r_{ij} = \frac{x_{ij}}{\sqrt{\sum_{i=1}^{m} x_{ij}^2}}, \tag{21}$$

and the weighted normalized matrix is defined as:

$$v_{ij} = w_j \cdot r_{ij}, \tag{22}$$

where w_j is the weight of criterion j.

The ideal (A_j^+) and negative-ideal (A_j^-) solutions are determined based on the criterion type. Since all criteria in this study are of the cost type (i.e., lower values are preferred):

$$A_j^+ = \min_i v_{ij}\ , A_j^- = \max_i v_{ij}. \tag{23}$$

The distances to the ideal and negative-ideal solutions are calculated as:

$$S_i^+ = \sqrt{\sum_{j=1}^{n} \left(v_{ij} - A_j^+\right)^2}, S_i^- = \sqrt{\sum_{j=1}^{n} \left(v_{ij} - A_j^-\right)^2}, \tag{24}$$

where S_i^+ and S_i^- are the Euclidean distances in the n-dimensional criteria space.

The Closeness Coefficient for each alternative is defined as:

 doi:10.20944/preprints202604.2108.v1

$$C_{k\_i} = \frac{s_i^-}{s_i^+ + s_i^-}. \quad (25)$$

This coefficient ranges from 0 to 1, where 1 corresponds to the ideal solution and 0 corresponds to the worst solution. It represents the TOPSIS score for each alternative.

Thus, based on the TOPSIS score, the engine operating lines are ranked, and the most efficient solutions are identified.

3. Results and Discussion

3.1. Building of Engine Operating Lines

The first step is to identify the engine operating modes at which the engine can be efficiently used within a PHEV configuration. These modes may lie along specific engine operating lines (e.g., curves 1–8 in Figure 6a or curves 1–8k in Figure 6b), which are located within a defined region of the engine map.

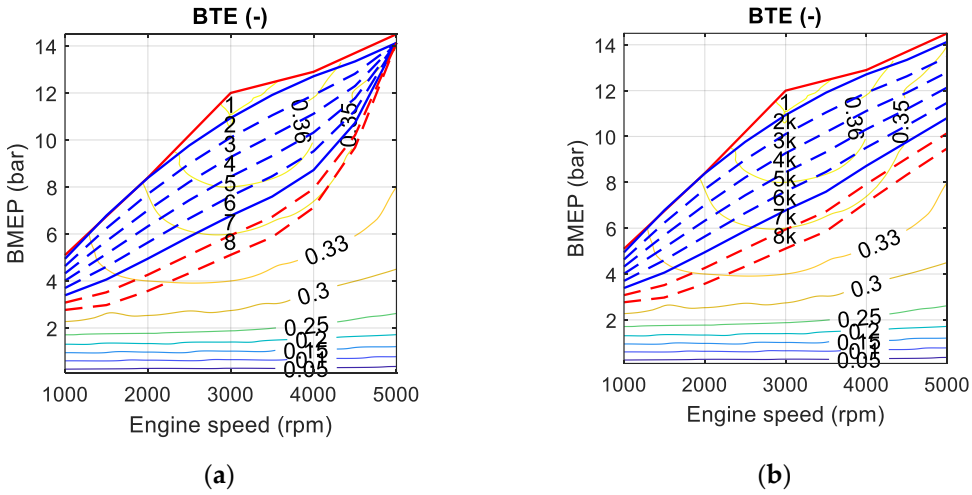

(**a**) (**b**)

Figure 6. Hydrogen engine operating lines for constant (a) and variable (b) maximum engine power.

At the upper boundary, the engine operating region is limited by EOL 1, which passes through the area of minimum fuel consumption. Since this curve initially exhibits a jagged shape, it is smoothed using a second-degree polynomial. This smoothing reduces the adverse effects of torque fluctuations on engine operation by minimizing the root-mean-square deviation.

At the lower boundary, the engine operating region is defined by EOL 8 (Figure 6a) and EOL 8k (Figure 6b), which are determined with the objective of minimizing NOx emissions. Two approaches are considered. In the first approach, the engine's maximum power is fixed at 58 kW, regardless of the EOL used. In the second approach, the engine's maximum power varies within the range of 39 kW to 50 kW.

To determine the position of EOL 8 in Figure 6a, the following method is applied. The engine speed range on the NOx map is divided into four intervals with a step of 1000 rpm, while the BMEP range is divided into intervals with a step of 1 bar (Figure 7a). By connecting the nodal points, a set of curves is obtained. To avoid sharp transitions and ensure stable engine operation, the maximum change in BMEP between adjacent points is limited to 4 bar. This constraint significantly reduces the number of feasible curves. A second constraint is imposed on the maximum BMEP at 5000 rpm, corresponding to an engine power of 58 kW.

As a result of this NOx map segmentation, 1,964 curves are obtained, shown as gray lines in Figure 7a. For each curve, the average NOx emissions are calculated as:

$$m_{NOx\_av} = \frac{1}{\sum_{i=1}^{5} P_i} \sum_{i=1}^{5} m_{NOxi} P_i, \quad (26)$$

 doi:10.20944/preprints202604.2108.v1

where m_{NOxi} and P_i are the NOx emissions and engine power at the given mode, respectively. The curves are then ranked based on m_{NOx_av}. At a power constraint of 58 kW, the minimum value of m_{NOx_av} is 0.37 g/kWh.

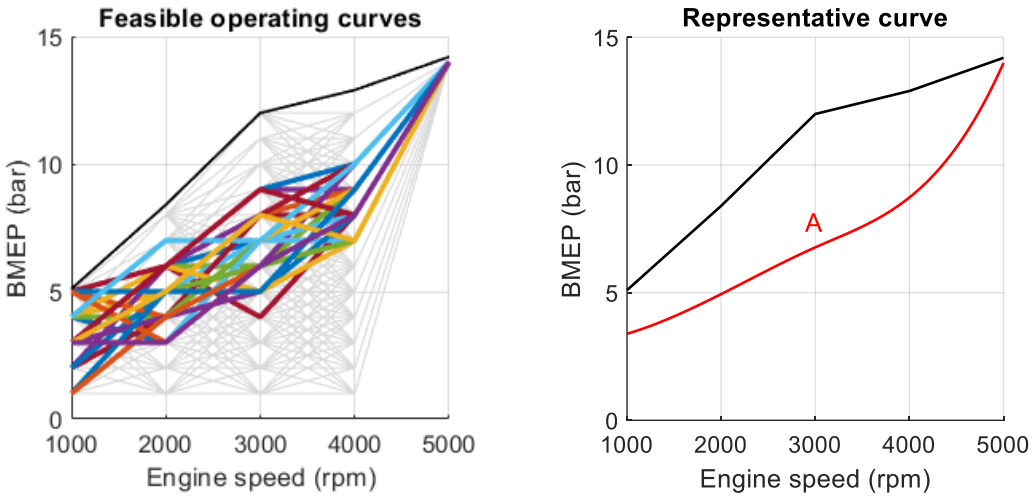

(**a**) (**b**)

Figure 7. Results of constructing hydrogen engine operating lines based on minimizing NOx emissions with a fixed maximum power: (a) 200 feasible curves with minimal average NOx emissions within a 5% deviation; (b) representative curve A obtained by averaging the 200 curves. .

Since the curve corresponding to the minimum m_{NOx_av} may exhibit discontinuities (i.e., noise), a set of feasible curves is selected whose deviation from m_{NOx_av} does not exceed 5%. These curves are then averaged to obtain a representative solution. In this study, 200 curves are selected (highlighted in Figure 7a), and their average yields curve *A*, shown in Figure 7b. Curve A corresponds to EOL 6 in Figure 6a.

The BMEP range between the engine operating lines corresponding to maximum BTE and minimum NOx emissions (EOL 1 and EOL 6 in Figure 6a) is divided into five equal intervals at each engine speed, resulting in EOL 2–5. To explore a broader spectrum of engine operating lines, this range is proportionally extended by adding EOL 7 and EOL 8, which are located in the lower-load region associated with reduced NOx emissions.

The constraint on maximum engine power limits the achievable reduction in average NOx emissions (Figure 8). For example, Figure 8 shows that at a maximum power of 58 kW, the minimum m_{NOx_av} is 0.37 g/kWh, whereas at a maximum power of 45 kW, the value decreases to 0.031 g/kWh—nearly 12 times lower.

In this context, the second approach with variable maximum power is investigated (Figure 6b). In this case, the corresponding curves 2–8 and 2k–8k coincide in the speed range from 1000 rpm to 4000 rpm. Between 4000 rpm and 5000 rpm, the maximum power for curve 8k decreases to 39 kW. The selection of maximum power for EOL 8k is based on data reported in [34,37] for PHEVs with similar parameters. The resulting range from 58 to 39 kW is then divided into seven intervals, forming the maximum power values for EOL 2k–7k.

3.2. Influence of Engine Operating Line Selection on PHEV Powertrain Parameters

The PHEV powertrain was simulated in charge-sustaining mode under the WLTC conditions. The mathematical model used the parameters and coefficients listed in Table 3. The battery state of charge was maintained within a range between SOC_{min} and SOC_{CS_max}. The lower limit was set to SOC_{min}=0.2, while SOC_{CS_max} varied between 0.25 and 0.4 in increments of 0.05. These SOC limits are consistent with values reported in [6,24,29,43,55] for PHEV applications.

 doi:10.20944/preprints202604.2108.v1

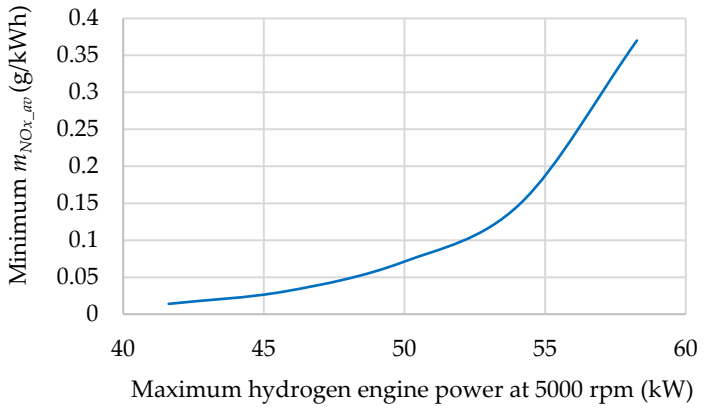

Figure 8. Effect of maximum hydrogen engine power on the minimal m_{NOx_av}.

Table 3. Parameters and coefficients used for PHEV powertrain simulation.

Parameter	Value
Vehicle mass	2705 kg
Vehicle width x height	2.25 m x 2.0 m
Frontal area filling factor	0.78
Rolling resistance coefficient	0.010
Aerodynamic drag coefficient	0.3
Maximum recuperation power	40 kW
Recuperation efficiency	0.85
Initial SOC	0.2
Minimum SOC	0.2
Maximum SOC in CS mode	0.25 – 0.4
Maximum discharge current	183 A
Maximum charge current	36.6 A

An example of the calculated operating modes of the engine, generator, and motor for EOL 1 with $SOC_{CS\_max} = 0.3$ is shown in Figure 9. The distribution of operating modes in the motor map is primarily determined by the test cycle parameters, vehicle mass, and transmission characteristics. In the engine and generator maps, the starting, braking, and load operation modes can be identified. In this case, the engine operating points lie along EOL 1 (see Figure 6).

The regulation of the engine's target power and speed is primarily achieved by adjusting the generator torque. As a result, the generator operating points exhibit some dispersion on its map, reflecting system control behavior. When the engine is disconnected to accelerate its deceleration, the generator produces a negative torque proportional to the engine speed. Consequently, the generator operating points during engine braking form a sloped linear trend.

 doi:10.20944/preprints202604.2108.v1

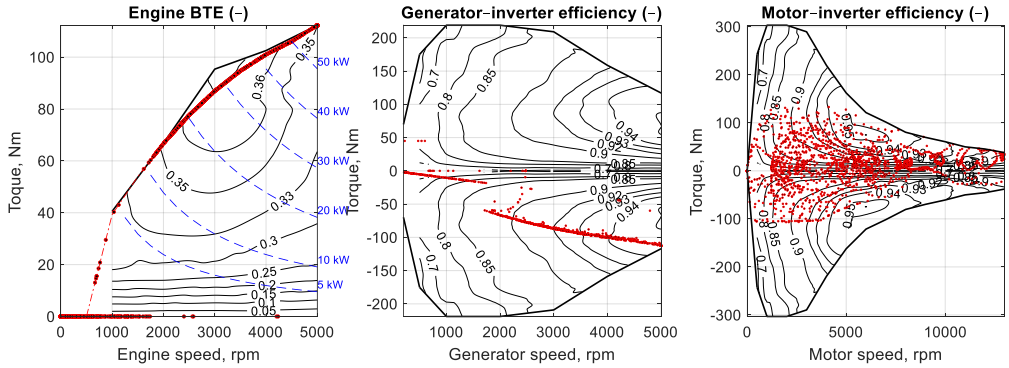

Figure 9. Calculated operating modes of the engine, generator, and motor for EOL 1 with SOC_{CS_max}.

Figure 10 compares the target engine torque T_{e_tar} and target engine speed $n_{targ,}$ required to satisfy the WLTC cycle conditions based on power balance of the PHEV powertrain components, with the corresponding calculated engine torque T_e and speed n, which also account for the rotational inertia of the engine and generator. The results show good agreement.

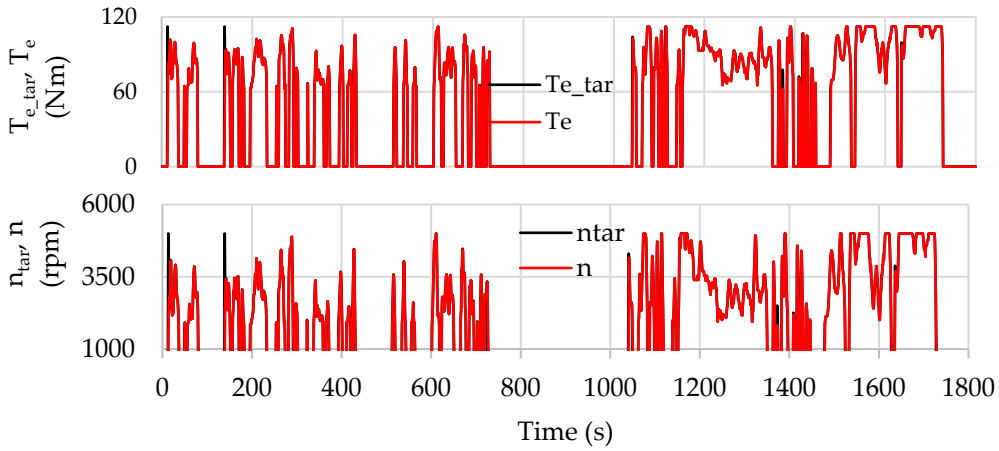

Figure 10. Calculated engine torque and speed under WLTC conditions using EOL 1 and SOC_{CS_max} = 0.3.

The influence of hydrogen engine operating line selection on the powertrain parameters is shown in Figure 11a for constant maximum power and in Figure 11b for variable maximum power. For this analysis, EOL 1, EOL 6 (6k) are selected, corresponding to maximum brake thermal efficiency and minimum NOx emissions, respectively.

From Figure 11, it is evident that the use of EOL 6 and EOL 6k reduces the engine torque T_e in several WLTC operating modes, which requires higher engine speeds n to maintain the same power output as with EOL 1. This results in a slight reduction in engine BTE, while NOx emissions are significantly reduced. These effects are most pronounced for EOL 6k under high-load (maximum torque) conditions.

In the considered PHEV architecture, the generator is directly coupled to the internal combustion engine shaft; therefore, its speed equals the engine speed. When using EOL 6 and EOL 6k, the generator operating points lie within a region of higher combined generator–inverter efficiency η_{GI} compared to EOL 1. This partially compensates for the reduction in engine BTE, thereby increasing the overall efficiency of the engine-generator-inverter system for EOL 6 and EOL 6k.

 doi:10.20944/preprints202604.2108.v1

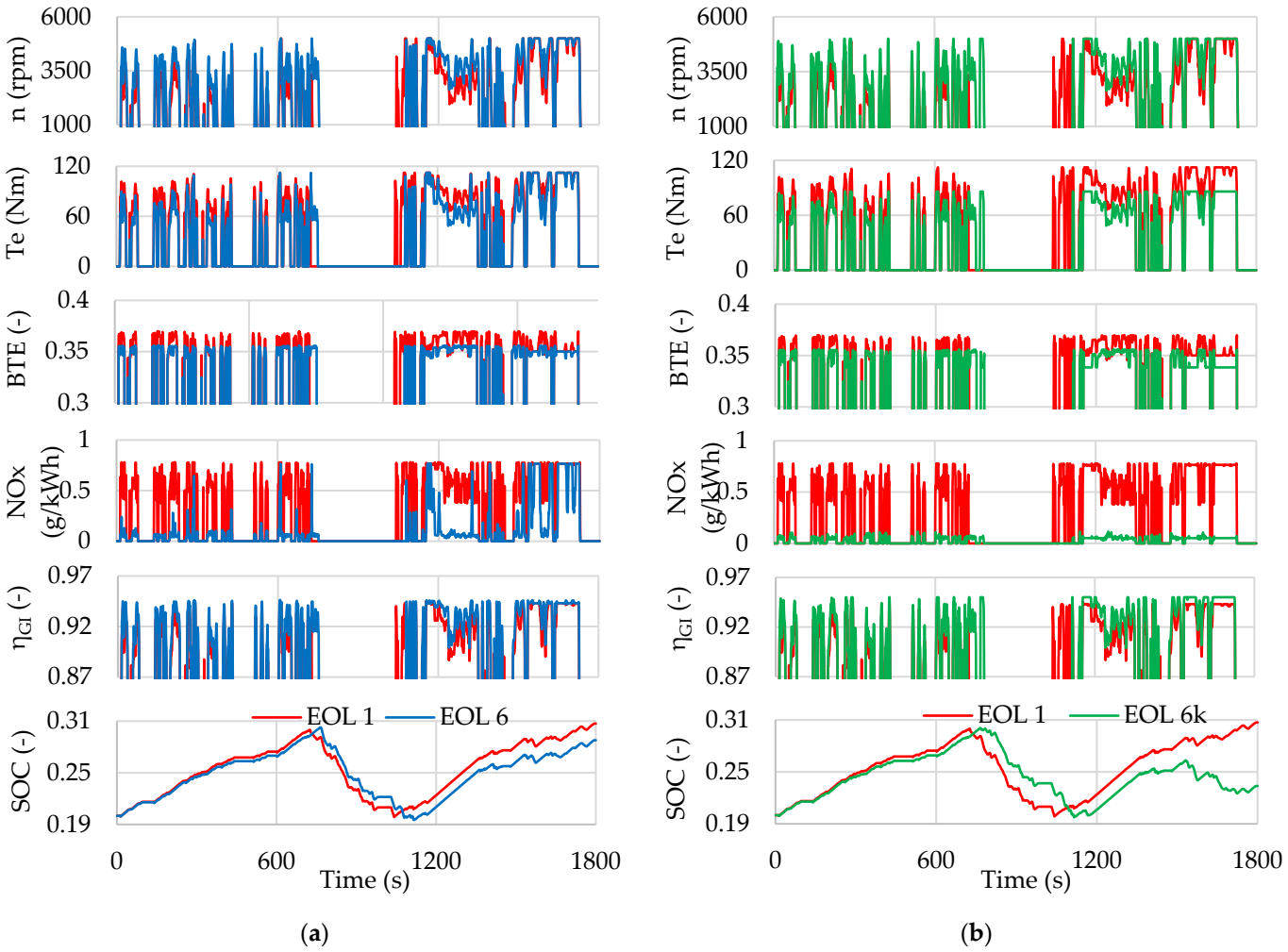

Figure 11. Parameters of the hydrogen engine, generator, and battery under WLTC cycle conditions using EOL 1 and EOL 6 (a), and EOL 1 and EOL 6k (b). SOC_{CS_max} = 0.3.

It should be noted that achieving the target power using EOL 6 and EOL 6k requires accelerating the engine to higher speeds than with EOL 1. Due to the engine's rotational inertia, this acceleration takes slightly longer and requires additional kinetic energy , resulting in a minor increase in the time required to charge the battery to the SOC_{CS_max}. For EOL 6k, the reduced maximum engine power leads to higher battery energy consumption and a faster battery discharge rate.

The time distribution of hydrogen engine operating parameters using EOL 1, EOL 6 and EOL 6k is shown in Figure 12. With EOL 1, the engine operates most frequently in the speed range of 2000–4000 rpm, while with EOL 6 and EOL 6k, the main operating range shifts to 2500–4500 rpm. The highest frequency of high-speed operation (23% of total engine operating time) is observed with EOL 6k.

With EOL 1, the engine operates mostly at torques from 70 Nm to 106 Nm, whereas for EOL 6 and EOL 6k, the majority of operation occurs in the ranges of 50–100 Nm and 50–90 Nm, respectively. For EOL 6k, a significant share of operation occurs around 85 Nm, accounting for 29% of the total engine operating time.

Using EOL 1, the engine operates with a BTE range of 35%–37% for approximately 20% and 25% more of the total engine operating time compared to EOL 6 and 6k, respectively. In contrast, the share of operating modes with relatively high NOx emissions (0.5 g/kWh–0.8 g/kWh) is 78% for EOL 1, whereas it decreases to approximately 14% for EOL 6 and becomes zero for EOL 6k.

Preprints.org (www.preprints.org) | NOT PEER-REVIEWED | Posted: 30 April 2026 doi:10.20944/preprints202604.2108.v1

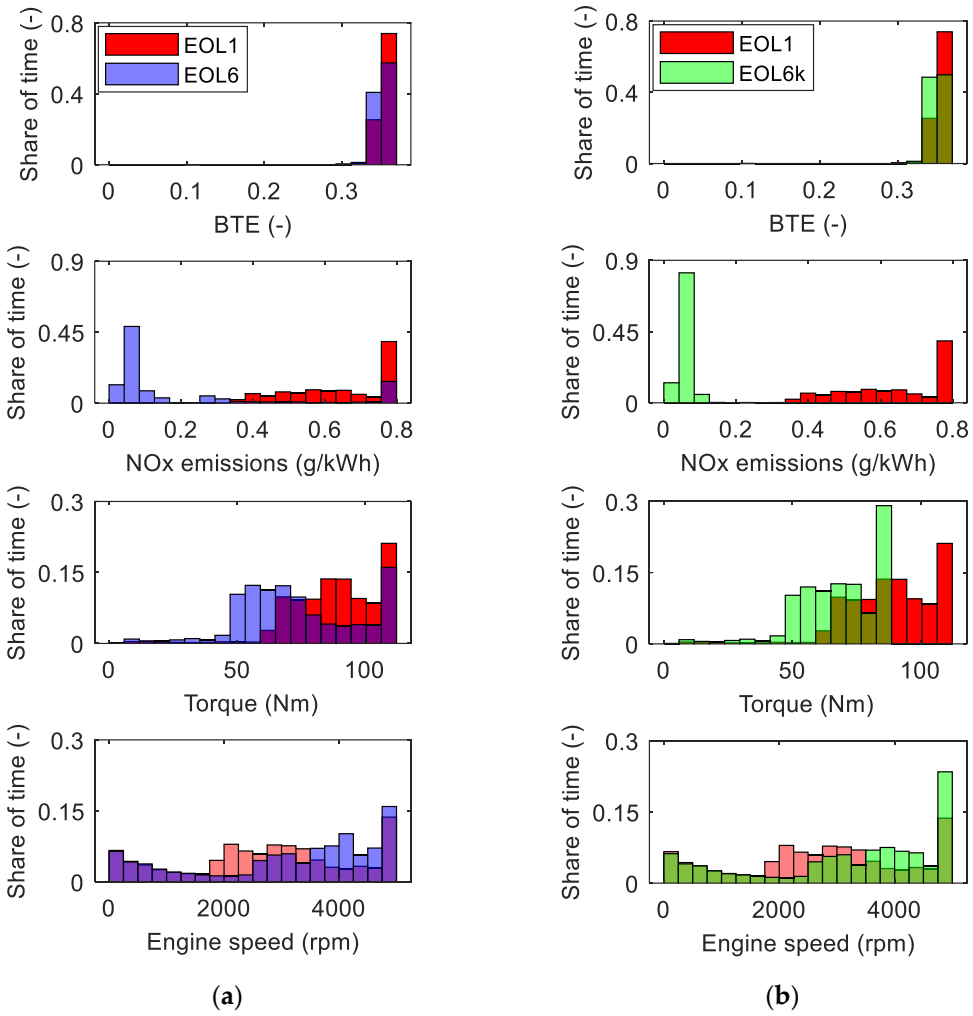

Figure 12. Distribution of hydrogen engine, generator, and battery parameters using EOL 1 and EOL 6 (a), and EOL 1 and EOL 6k (b). .

The results demonstrate a significant influence of the EOL selection on engine and hybrid powertrain component behavior under WLTC conditions. A comprehensive assessment of this influence can be carried out using a set of performance criteria.

3.3. Analysis of Engine Operating Lines Effectiveness Using a Criteria-Based Assessment

3.3.1. Performance Criteria

The effectiveness of different EOLs was evaluated using cycle-integrated criteria over the WLTC. The primary criteria selected were specific fuel energy consumption (J/km) ($C_1 = E_{H_{2\_km}}$) and specific NOx emissions (g/km) ($C_2 = m_{NOx\_km}$).

Section 3.2 shows that minimizing NOx leads to increased engine speed, reduced engine torque, and changes in generator and battery operating parameters. To account for these effects, it is appropriate to include additional criteria related to reliability and system performance.

A literature review identified several criteria used in the development and optimization of hybrid vehicle EMS, including the number of engine start–stops [6], tire/road noise [20,56], and battery aging [21]. Preliminary calculations in this study indicated low sensitivity of both the number of start–stops and battery aging (evaluated using the model from [21]) to the EOL selection within the considered RB EMS. Therefore, these criteria were not included in the subsequent comprehensive evaluation.

 doi:10.20944/preprints202604.2108.v1

The assessment of tire/road noise requires experimental data specific to the investigated vehicle. Since such data were not available for the PHEV considered in this study, this criterion was also excluded.

Instead, we propose proxy criteria C_3 – C_5 to account for the effects of EOL selection on component wear, mechanical fatigue, and noise, vibration, and harshness (NVH) excitation (Table 4). The values of these criteria are functionally related to different physical phenomena and vary significantly with changes in the EOL (see Section 3.1.2). Therefore, they can be used for a comparative evaluation of the considered alternatives.

Table 4. Proxy criteria used used for reliability and NVH evaluation.

Physical phenomenon	Physical basis, criterion
Wear (tribological)	According to Archard's law [57], wear is proportional to the product of contact load and sliding distance. In an internal combustion engine, the contact load can be represented by the total friction mean effective pressure (TFMEP), while the sliding distance per unit time is proportional to engine speed n. According to Heywood [58], for SI engines: $$\mathrm{TFMEP} = 0.97 + 0.15\left(\frac{n}{1000}\right) + 0.05\left(\frac{n}{1000}\right)^2, \quad (27)$$ where n is the engine speed. The wear criterion is defined as: $$C_3 = \frac{1}{T}\int_0^T TFMEP \cdot n \, dt, \quad (28)$$ where T is the total duration of the WLTC and t denotes time.
Mechanical fatigue	High-cycle fatigue damage follows Basquin's law (Miner's rule formulation) [59]: $$D_{mech} = f\left(\sigma_a^{m_1}\right), \quad (29)$$ where σ_a is the stress amplitude and m_1 is the fatigue exponent (slope of the S–N curve). For typical engine materials such as steel or cast iron, $m_1 \approx$ 8–20 [60 Stephens, 61 Dowling]. Assuming that the stress amplitude is proportional to BMEP [58], a commonly used indicator of engine load, the damage rate can be expressed as: $$D_{mech} \propto BMEP^{m_1}. \quad (30)$$ The mechanical fatigue criterion is then defined as: $$C_4 = \frac{1}{T}\int_0^T BMEP^{\,m_1} dt. \quad (31)$$
NVH excitation	Vibration energy is proportional to the square of the excitation force [62]: $$E_{vib} \propto F_{exc}^2, \quad (32)$$ where F_{exc} is the excitation force. In internal combustion engines, excitation forces are mainly caused by unbalanced inertial forces and moments [58]. The second-order inertia force is proportional to the square of engine speed: $$F_{exc} \propto n^2. \quad (33)$$ Thus: $$E_{vib} \propto n^4. \quad (34)$$ The NVH excitation criterion is defined as:

 doi:10.20944/preprints202604.2108.v1

$$C_5 = \frac{1}{T}\int_0^T n^4\, dt. \tag{35}$$

3.3.2. Influence of Engine Operating Line Selection on the Selected Criteria

The influence of the EOL selection on the selected criteria can be conveniently evaluated using normalized values (Figure 13):

$$\overline{C_j} = \frac{c_j}{c_{j\_max}}, \tag{36}$$

where C_j and C_{j_max} are the current and maximum values of the j-th criterion for a given EOL, respectively.

This influence was analyzed for the cases of constant maximum power (EOL 1–8, Figure 13a) and variable maximum power (EOL 1–8k, Figure 13b).

From Figure 13, it is evident that EOL selection significantly affects the relative values of criteria C_2–C_5. For the constant maximum power case (Figure 13a), a sequential shift from EOL 1 to EOL 8 leads to a reduction in NOx emissions by a factor of 2.4 and a reduction in mechanical fatigue by a factor of 1.56. At the same time, wear increases by a factor of 1.4, and NVH excitation increases by a factor of 1.62. Fuel energy consumption remains practically unchanged in this case.

For the variable power variant (Figure 13b), the influence of the EOL selection on relative criterion values is even more pronounced. Moving from EOL 1 to EOL 8k reduces NOx emissions by a factor of 43, approaching zero, and decreases mechanical fatigue by a factor of 14.5. Meanwhile, wear increases by a factor of 1.45, and NVH excitation increases by a factor of 1.82. Fuel energy consumption decreases by approximately 11%.

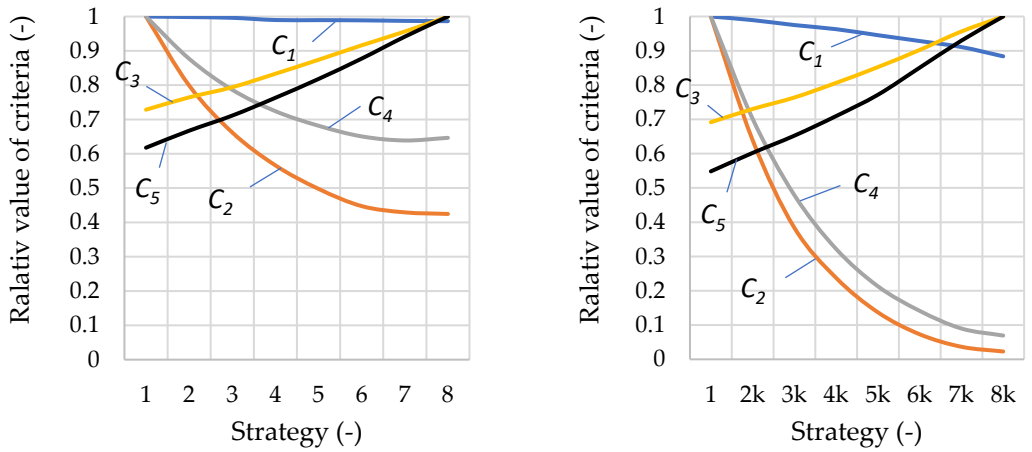

Figure 13. Influence of engine operating line selection on relative criterion values C_1 – C_5 with SOC_{CS_max} = 0.3 (C_1 – fuel energy consumption, C_2 – specific NOx emissions, C_3 – wear, C_4 – mechanical fatigue, C_5 – NVH excitation).

The conflicting trends of the criteria observed when moving sequentially from EOL 1 to EOL 8 (or from EOL 1 to EOL 8k) highlight the need for a comprehensive evaluation using modern methods that enable normalization of the criteria and ranking of alternatives.

3.3.3. Determination of Criteria Weights

The weights for criteria C_1 – C_5 were determined using the AHP method (see Section 2.3). In accordance with this method, a hierarchical model was constructed, including the overall decision problem, the criteria, and the alternatives to be compared. Figure 14 shows the hierarchical model for the case with fixed maximum engine power. The model for the variable maximum power case is structured in a similar way.

 doi:10.20944/preprints202604.2108.v1

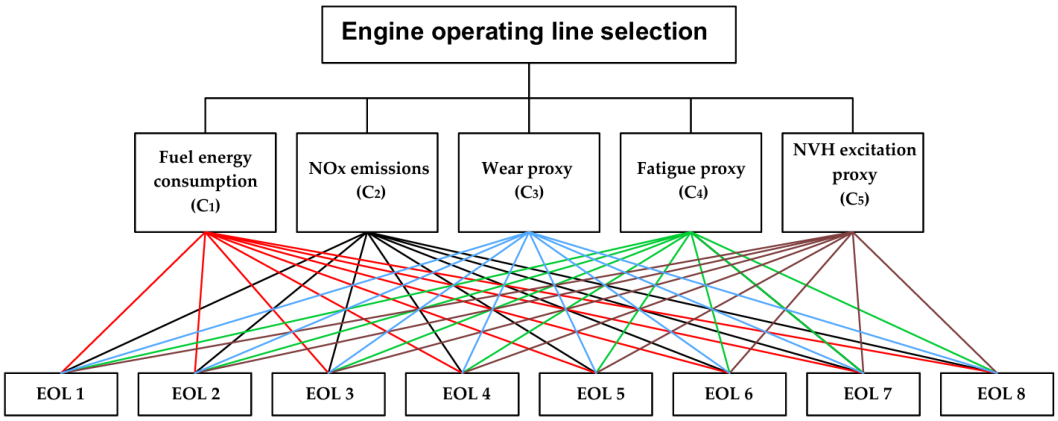

Figure 14. Hierarchical structure of the analyzed problem.

The results of the pairwise comparison of criteria using Saaty's scale [50] are presented in Table 5. The table is constructed based on information regarding the relative importance of various criteria used in the multi-criteria optimization of sustainable energy systems [47–49,52,63].

In the comparative evaluation of the criteria, fuel energy consumption (C_1) is considered equally important as NOx emissions (C_2). The next most important criterion is engine wear (C_3), as this factor acts continuously and leads to cumulative damage. Mechanical fatigue (C_4) becomes critical under high cyclic loads; however, in this engine, the maximum BMEP is approximately 15 Bar, which is significantly lower than in a base gasoline engine (~20 Bar). Therefore, this criterion is assigned lower importance. NVH excitation (C_5) primarily affects driving comfort and is assigned the lowest importance.

Table 5. Pairwise Criteria Comparison.

Criteria	C_1	C_2	C_3	C_4	C_5	Weights
C_1	1	1	2	3	4	0.3192
C_2	1	1	2	3	4	0.3192
C_3	1/2	1/2	1	2	3	0.184
C_4	1/3	1/3	1/2	1	2	0.1093
C_5	1/4	1/4	1/3	1/2	1	0.0683

The calculated AHP weights are shown in Table 5. It can be seen that the combined weight of fuel economy and emissions criteria is approximately 64%, while the remaining 36% accounts for reliability and comfort-related criteria. This distribution aligns well with the data reported in [47–49,52,63].

The Consistency Ratio (CR) is 0.0184, indicating acceptable level of consistency in the constructed pairwise comparison matrix.

3.3.4. Ranking of Engine Operating Lines

The TOPSIS method is used to rank the EOLs. In the calculations, the criteria weights w_j obtained with the use of the AHP method (see Table 5), were applied. In this method, the performance indicator is the Closeness Coefficient (see Section 2.3), with higher values corresponding to better alternatives.

Figure 15 shows the Closeness Coefficient values for EOL variants with constant and variable maximum power. Here, SOC_{CS_max} is varied from 0.25 to 0.4 (Figure 15a), and the weighs are varied within ±20% (Figure 15b). When a selected weight w_j is increased by 20%, the remaining weights are proportionally reduced, and vice versa, while maintaining the condition $\sum_{j=1}^{n} w_j = 1$.

 doi:10.20944/preprints202604.2108.v1

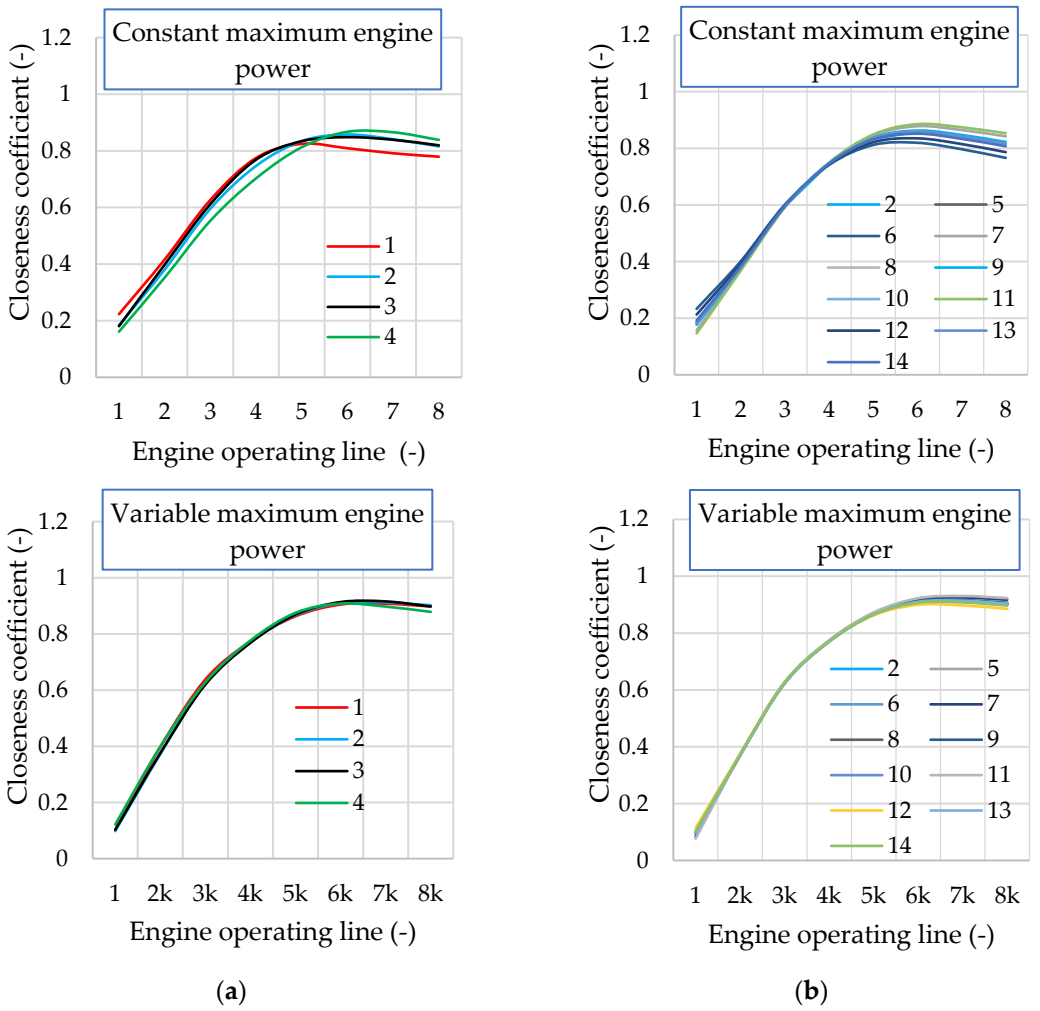

Figure 15. TOPSIS Closeness Coefficient results for different engine operating lines: (a) variation of SOC_{CS_max} from 0.25 to 0.4; (b) variation of weights w_j ±20% from the values in Table 5 with SOC_{CS_max} =0.3. 1 – SOC_{CS_max} = 0.25, 2 – SOC_{CS_max} = 0.3, 3 – SOC_{CS_max} = 0.35, 4 – SOC_{CS_max} = 0.4, 5 – w_1-20%, 6 – w_2 – 20%, 7 – w_3 – 20%, 8 – w_4 – 20%, 9 – w_5 – 20%, 10 – w_1 + 20%, 11 – w_2 + 20%, 12 – w_3 + 20%, 13 – w_4 + 20%, 14 – w_5 + 20%.

It can be seen that for EOL 5 and EOL 6 in the constant maximum power variant, and EOL 6k and EOL 7k in the variable maximum power variant, the highest Closeness Coefficient values are achieved. Variations in SOC_{CS_max} and the weights over a wide range have practically no effect on the results, indicating the high stability of the ranking.

The calculated fuel energy consumption and NOx emissions for EOL 1, EOL 5, EOL 6, EOL 6k, and EOL 7k are shown in Figure 16. It is evident that for these EOLs, fuel consumption varies within a relatively narrow range of about 10%. At the same time, using EOL 5, EOL 6, EOL 6k, and EOL 7k results in a significant reduction in NOx emissions compared to EOL 1. For EOL 6k and 7k, NOx emissions can be reduced well below the Euro 6 limits without additional exhaust gas aftertreatment. When using EOL 6, it is also possible to meet Euro 6 limits at SOC_{CS_max} =0.4; however, in this case, NOx emissions are at the borderline of the standard, increasing the risk of exceeding the limits and requiring exhaust gas aftertreatment.

Thus, EOL 5 and 6 can be recommended for a hydrogen engine with fixed maximum power of 58 kW and exhaust gas aftertreatment. In contrast, EOL 6k and EOL 7k are recommended for a hydrogen engine without aftertreatment. In this case, the maximum engine power would need to be reduced from 58 kW to 42 kW–45 kW, which may lead to reduced PHEV efficiency during dynamic driving conditions.

 doi:10.20944/preprints202604.2108.v1

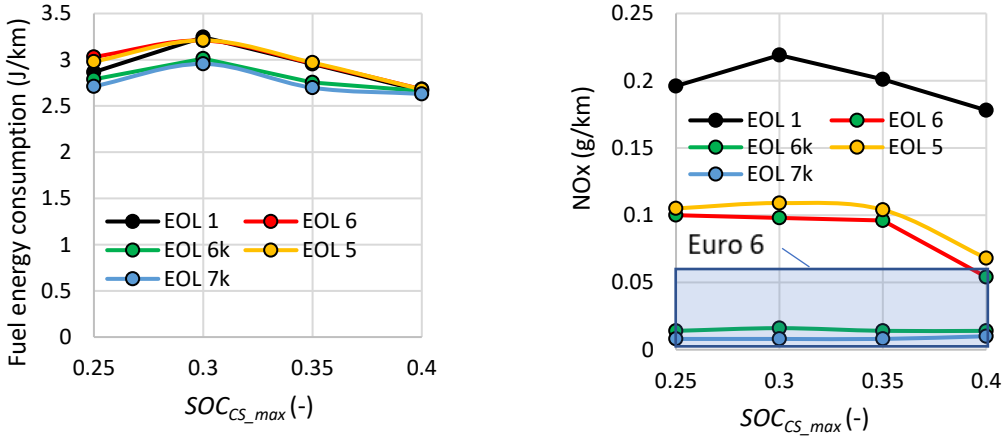

(**a**) (**b**)

Figure 16. Fuel energy consumption (a) and NOx emissions (b) for SOC_{CS_max} varying from 0.25 to 0.4 and applying EOL 1, EOL 5, EOL 6, EOL 6k, and EOL 7k.

The main outcome of this study is that compliance with stringent emission regulations for an engine within a PHEV, while maintaining acceptable fuel economy and reliability, can be achieved solely through the selection of appropriate engine operating modes without modifying its baseline design parameters or calibration settings.

4. Conclusions

The study justifies the selection of the most efficient engine operating lines for a hydrogen engine within a PHEV. The main findings are as follows:

1. A backward-type mathematical model of PHEV operation is developed, incorporating a rule-based EMS strategy and accounting for the rotational inertia of the engine and generator components.
2. A methodology is proposed for building hydrogen engine operating lines in the case of a rule-based EMS, enabling the minimization of NOx emissions while considering maximum engine power limitations. Using this methodology, a set of 15 engine operating lines is obtained for both constant and variable maximum engine power variants.
3. The parameters of the hydrogen engine, generator, and battery are analyzed under the WLTC test cycle when applying engine operating lines aimed at achieving maximum BTE (EOL 1) and minimizing NOx emissions (EOL 6, EOL 6k). It is shown that using EOL 6 and EOL 6k reduces engine torque while simultaneously increasing engine speed compared to EOL 1. The resulting decrease in BTE is compensated by the increased combined efficiency of the generator and inverter.
4. For a comparative evaluation of engine operating lines, a set of five performance criteria is proposed, including fuel energy consumption, NOx emissions, wear, mechanical fatigue, and NVH excitation. Weights for these criteria were determined using the AHP method.
5. Engine operation is simulated under WLTC conditions to calculate performance criteria for 15 EOLs in both constant and variable maximum engine power variants. It is shown that when moving sequentially from strategies prioritizing maximum BTE to strategies minimizing NOx, mechanical fatigue decreases while wear and NVH increase. This effect is more pronounced for the variable maximum power variant.
6. Ranking the hydrogen engine operating lines using the TOPSIS method identified the most effective operating lines. The sensitivity analysis showed that the results are robust with respect to variations in weighting factors and the maximum SOC in CS mode. The use of these operating

 doi:10.20944/preprints202604.2108.v1

lines enables NOx emissions to be reduced significantly below Euro 6 limits without exhaust gas aftertreatment.

Author Contributions: Conceptualization, O.O. and R.H.; methodology, O.O.; software, O.O.; validation, O.O.; formal analysis, O.O. and R.H.; investigation, O.O.; resources, O.O.; data curation, O.O. and R.H.; writing—original draft preparation, O.O. and R.H.; writing—review and editing, O.O. and R.H.; visualization, O.O.; supervision, R.H.; project administration, R.H. All authors have read and agreed to the published version of the manuscript.

Data Availability Statement: The original contributions presented in the study are included in the article; further inquiries can be directed to the corresponding author.

Acknowledgments: The authors express their gratitude to the leadership of the University of Applied Sciences Cologne and the Faculty of Automotive Systems and Production for providing access to the Matlab software license and facilitating the research and computational aspects of this study.

Conflicts of Interest: The authors declare no potential conflicts of interest with respect to the research, authorship, and/or publication of this article.

Abbreviations

The following abbreviations are used in this manuscript:

AC	Alternating current
AHP	Analytic Hierarchy Process
BMEP	Brake mean effective pressure
BTE	Brake thermal efficiency
CS	Charge-sustaining
DC	Direct current
EMS	Energy management system
EOL	Engine operating line
HEV	Hybrid electric vehicle
NOx	Nitrogen oxides
NVH	Noise, vibration, and harshness
OB EMS	Optimization-based energy management system
PHEV	Plug-in hybrid electric vehicle
RB EMS	Rule-based energy management system
SOC	State of charge
TFMEP	Total friction mean effective pressure
TOPSIS	Technique for Order Preference by Similarity to Ideal Solution
WLTC	Worldwide Harmonized Light Vehicles Test Cycle

References

1. European Commission. *A Hydrogen Strategy for a Climate-Neutral Europe.* COM(2020) 301 final; European Commission: Brussels, Belgium, 2020. Available online: https://eur-lex.europa.eu/legal-content/EN/TXT/?uri=CELEX:52020DC0301 (accessed on 1 October 2025).
2. EY. *Hyvolution 2025—European Hydrogen Market Outlook.* EY: Paris, France, 2025. Available online: https://www.ey.com/content/dam/ey-unified-site/ey-com/fr-fr/insights/climate-change-sustainability-services/documents/ey-hyvolution-ey-european-hydrogen-20250214.pdf (accessed on 1 October 2025).

 doi:10.20944/preprints202604.2108.v1

3. Reuters. Germany Proposes Annual Fee to Kick-Start Hydrogen Pipeline Network. 26 March 2025. Available online: https://www.reuters.com/business/energy/germany-proposes-annual-fee-kick-start-hydrogen-pipeline-network-2025-03-26 (accessed on 1 October 2025).
4. Regulation (EU) 2019/631 of the European Parliament and of the Council of 17 April 2019 on Setting CO_2 Emission Performance Standards for New Passenger Cars and for New Light Commercial Vehicles, and Amending Regulation (EC) No 715/2007 and (EC) No 595/2009. *Off. J. Eur. Union* 2019, L111, 25 April 2019. Available online: https://eur-lex.europa.eu/legal-content/EN/TXT/?uri=CELEX%3A32019R0631 (accessed on 1 October 2025).
5. Regulation (EU) 2023/851 of the European Parliament and of the Council of 19 April 2023 Amending Regulation (EU) 2019/631 as Regards Strengthening the CO_2 Emission Performance Standards for New Passenger Cars and New Light Commercial Vehicles. *Off. J. Eur. Union* 2023, L110, 19 April 2023. Available online: https://eur-lex.europa.eu/eli/reg/2023/851/oj/eng (accessed on 1 October 2025).
6. Chen, C.; Wang, X.; Xie, Z.; Lei, Z.; Shangguan, C. Research on Plug-in Hybrid Electric Vehicle (PHEV) Energy Management Strategy with Dynamic Planning Considering Engine Start/Stop. *World Electr. Veh. J.* **2024**, 15, 350.
7. Yang, C.; Du, X.; Wang, W.; Yuan, L.; Yang, L. Variable Optimization Domain-Based Cooperative Energy Management Strategy for Connected Plug-in Hybrid Electric Vehicles. *Energy* **2024**, 290, 130206.
8. Stepien, Z. Comprehensive Overview of Hydrogen-Fueled Internal Combustion Engines: Achievements and Future Challenges. *Energies* **2021**, 14, 6504.
9. Sun, Z.; Hong, J.; Zhang, T.; Sun, B.; Yang, B.; Lu, L.; Li, L.; Wu, K. Hydrogen Engine Operation Strategies: Recent Progress, Industrialization Challenges, and Perspectives. *Int. J. Hydrogen Energy* **2023**, 48(1), 366–392.
10. Gao, W.; Fu, Z.; Li, Y.; Li, Y.; Zou, J. Progress of Performance, Emission, and Technical Measures of Hydrogen Fuel Internal-Combustion Engines. *Energies* **2022**, 15, 7401.
11. Verhelst, S. Recent Progress in the Use of Hydrogen as a Fuel for Internal Combustion Engines. *Int. J. Hydrogen Energy* **2014**, 39, 1071–1085.
12. Töpfer, G.; et al. Single-Cylinder- and Multi-Cylinder-Engine Investigation on TCG 7.8 H_2—Further Development Steps for the Realization of a H_2 Engine for NRMM. In *Heavy-Duty-, On- und Off-Highway-Motoren 2023. HDENGI 2022. Proceedings*; Heintzel, A., Ed.; Springer Vieweg: Wiesbaden, Germany, 2025;
13. Pirkl, R.; D'Onofrio, M.; Kapusta, L.; Herrmann, D. H_2 Direct Injection System for Heavy Duty ICE in Transient On- & Off-Road Operation. In *Commercial Vehicle Technology 2022. ICVTS 2022. Proceedings*; Berns, K., Dressler, K., Kalmar, R., Stephan, N., Teutsch, R., Thul, M., Eds.; Springer Vieweg: Wiesbaden, Germany, 2022.
14. Broda, A.; et al. 4×2 Tractor with a Hydrogen Combustion Engine—Highest Performance with Lowest Emissions. In *Internationaler Motorenkongress 2023. Int.Engine.Congr. 2024. Proceedings*; Heintzel, A., Ed.; Springer Vieweg: Wiesbaden, Germany, 2024.
15. Lü, X.; Li, S.; He, X.H.; Xie, C.; He, S.; Xu, Y.; Fang, J.; Zhang, M.; Yang, X. Hybrid Electric Vehicles: A Review of Energy Management Strategies Based on Model Predictive Control. *J. Energy Storage* **2022**, 56, 106112.
16. Tran, D.; Vafaeipour, M.; Baghdadi, M.E.; Barrero, R.; Mierlo, J.V.; Hegazy, O. Thorough State-of-the-Art Analysis of Electric and Hybrid Vehicle Powertrains: Topologies and Integrated Energy Management Strategies. *Renew. Sustain. Energy Rev.* **2020**, 119, 109596.
17. Zhang, L.; Liu, W.; Qi, B. Innovation Design and Optimization Management of a New Drive System for Plug-in Hybrid Electric Vehicles. *Energy* **2019**, 186, 115823.
18. Huang, K.D.; Nguyen, M.-K.; Chen, P.-T. A Rule-Based Control Strategy of Driver Demand to Enhance Energy Efficiency of Hybrid Electric Vehicles. *Appl. Sci.* **2022**, 12, 8507.
19. Puma-Benavides, D.S.; Calderon-Najera, J.d.D.; Izquierdo Reyes, J.; Galluzzi, R.; Llanes-Cedeño, E.A. Methodology to Improve an Extended-Range Electric Vehicle Module and Control Integration Based on Equivalent Consumption Minimization Strategy. *World Electr. Veh. J.* **2024**, 15, 439.

 doi:10.20944/preprints202604.2108.v1

20. Zhang, S.; Wang, H.; Yang, C.; Ouyang, Z.; Wen, X. Optimization of Energy Management Strategy for Series Hybrid Electric Vehicle Equipped with Dual-Mode Combustion Engine Under NVH Constraints. *Appl. Sci.* **2024**, 14, 12021.
21. Anselma, P.; Kollmeyer, P.; Belingardi, G.; Emadi, A. Multitarget Evaluation of Hybrid Electric Vehicle Powertrain Architectures Considering Fuel Economy and Battery Lifetime. *SAE Tech. Pap.* 2020-37-0015, 2020.
22. Rana, B.L.; Shrestha, A.; Phuyal, S.; Mali, B.; Lakhey, O.; Maskey, R.K. Design and Performance Evaluation of Series Hybrid Electric Vehicle Using Backward Model. *J. Eng.* **2020**, 2020, 1095–1102.
23. He, H.; Shou, Y.; Song, J. An Improved A-ECMS Energy Management for Plug-in Hybrid Electric Vehicles Considering Transient Characteristics of Engine. *Energy Rep.* **2023**, 10, 2006–2016.
24. Liu, Y.; Ni, J.; Huang, R.; Shi, X.; Xu, Z.; Wang, Y.; Lu, Y. Optimization of Energy Management Strategy of a PHEV Based on Improved PSO Algorithm and Energy Flow Analysis. *Sustainability* **2024**, 16, 9017.
25. Feng, J.; Han, Z.; Wu, Z.; Li, M. A Dynamic ECMS Method Considering Vehicle Speed Pattern and Minimum Engine Operation Time for a Range-Extender Electric Vehicle. *IEEE Trans. Veh. Technol.* **2022**, 71, 4788–4800.
26. Tafel, S.; Martin, L. Development of a High-Performance Hydrogen Engine. In *2024 Stuttgart International Symposium on Automotive and Engine Technology*; Kulzer, A.C.; Reuss, H.C., Eds.; Springer Vieweg: Wiesbaden, Germany, 2024.
27. Körfer, T.; Durand, T.; Adomeit, P.; Blomberg, M.; Michelet, F.; Combemale, L.; Meyer, S. Design and Development of a High-Performance H_2 ICE for Upcoming Dakar Rally Championships—A Promotor of Carbon-Free Individual Mobility. In *Proceedings of the International Conference on Powertrain Systems for a Sustainable Future*; Institution of Mechanical Engineers, Ed.; CRC Press: London, UK, 2023.
28. He, X.; Maxwell, T.; Parten, M.E. Development of a Hybrid Electric Vehicle with a Hydrogen-Fueled IC Engine. *IEEE Trans. Veh. Technol.* **2006**, 55, 1693–1703.
29. Arsie, I.; Battistoni, M.; Brancaleoni, P.P.; Cipollone, R.; Corti, E.; Di Battista, D.; Millo, F.; Occhicone, A.; Peiretti Paradisi, B.; Rolando, L.; et al. A New Generation of Hydrogen-Fueled Hybrid Propulsion Systems for the Urban Mobility of the Future. *Energies* **2024**, 17, 34.
30. Beccari, S. On the Use of a Hydrogen-Fueled Engine in a Hybrid Electric Vehicle. *Appl. Sci.* **2022**, 12, 12749.
31. Martinez-Boggio, S.; Bibiloni, S.; Rivoir, F.; Irimescu, A.; Merola, S. Mitigating Power Deficits in Lean-Burn Hydrogen Engines with Mild Hybrid Support for Urban Vehicles. *Vehicles* **2025**, 7, 88.
32. Kyjovský, Š.; Vávra, J.; Bortel, I.; Toman, R. Drive Cycle Simulation of Light Duty Mild Hybrid Vehicles Powered by Hydrogen Engine. *Int. J. Hydrogen Energy* **2023**, 48, 16885–16896.
33. Machacek, D.T.; Yasar, N.O.; Huber, T.; Onder, C.H. Energy Management of Hydrogen Hybrid Electric Vehicles—A Potential Analysis. *Int. J. Hydrogen Energy* **2024**, 58, 1–13.
34. Bloch, P.; Mäurer, W.; Geiler, J.; Schünemann, E.; Kirzinger, M. Light Commercial Vehicle with a H_2 Engine Hybrid Powertrain. In *Proceedings of the Conference on Powertrains with Renewable Energy Carriers*; Stuttgart, Germany, 2023.
35. Geiler, J.N.; Springer, K.M.; Lorenz, T.; Blomberg, M.; Achenbach, J.; Bloch, P. H2 Engine Hybrid Powertrain for Future Light Commercial Vehicles. In *Internationaler Motorenkongress 2023*; Heintzel, A., Ed.; Springer Vieweg: Wiesbaden, Germany, 2024.
36. Fischer, M.; Sterlepper, S.; Pischinger, S.; Seibel, J.; Kramer, U.; Lorenz, T. Operation Principles for Hydrogen Spark Ignited Direct Injection Engines for Passenger Car Applications. *Int. J. Hydrogen Energy* **2022**, 47, 5638–5649.
37. Geiler, J.N.; Springer, K.M.; Bloch, P.; Kirzinger, M. Optimization of Combustion System, Emission Concept and Hybrid Operating Strategy for an LCV Powered by H2 Engine. In *Internationaler Motorenkongress 2024. Int.Engine.Congr. 2024. Proceedings*; Springer Vieweg: Wiesbaden, Germany, 2025.
38. Osetrov, O.; Haas, R. Simulation of Hydrogen Combustion in Spark Ignition Engines Using a Modified Wiebe Model. *SAE Tech. Pap.* 2024-01-3016, 2024.
39. Osetrov, O.; Haas, R. Modeling Homogeneous, Stratified, and Diffusion Combustion in Hydrogen SI Engines Using the Wiebe Approach. *Energies* **2025**, 18, 3004.

 doi:10.20944/preprints202604.2108.v1

40. Osetrov, O.; Haas, R. Selection of Injection Parameters in Hydrogen SI Engines Using a Comprehensive Criterion-Based Approach. *Vehicles* **2026**, 8, 14.
41. Sterlepper, S.; Fischer, M.; Claßen, J.; Huth, V. et al. 2021. Concepts for hydrogen internal combustion engines and their implications on the exhaust gas aftertreatment system. Energies **2021**, 14(23), 8166.
42. Burress, T.A.; Campbell, S.L.; Coomer, C.L.; Ayers, C.W.; Wereszczak, A.A.; Cunningham, J.P.; Marlino, L.D.; Seiber, L.E.; Lin, H.-T. Evaluation of the 2010 Toyota Prius Hybrid Synergy Drive System; ORNL/TM-2010/253; Oak Ridge National Laboratory: Oak Ridge, TN, USA, 2011.
43. Zhang, X. Design of Power Split Hybrid Powertrains with Multiple Planetary Gears and Clutches. Ph.D. Thesis, University of Michigan, Ann Arbor, MI, USA, 2015. Available online: https://deepblue.lib.umich.edu/handle/2027.42/111XXX.
44. Kim, N.; Rousseau, A.; Rask, E. Autonomie Model Validation with Test Data for 2010 Toyota Prius. *SAE Tech. Pap.* 2012-01-1040, 2012
45. Hu, L.; Zhang, D.; Huang, J.; Tian, Q.; Berecibar, M.; Zou, C. A Multi-Criteria Evaluation Framework for Adaptability of Hybrid Energy Storage System Energy Management Strategies to Dynamic Driving Style. *Appl. Energy* **2026**, 402, 127005.
46. Kinoti, E.; Mosetlhe, T.C.; Yusuff, A.A. Multi-Criteria Analysis of Electric Vehicle Motor Technologies: A Review. *World Electr. Veh. J.* **2024**, 15, 541.
47. Rivero-Iglesias, J.M.; Puente, J.; Fernandez, I.; León, O. A Novel Combined Hybrid Group Multi-Criteria Decision-Making Model for the Selection of Power Generation Technologies. *Systems* **2025**, 13, 742.
48. Hernández-Torres, J.A.; Sánchez-Lozano, D.; Sánchez-Herrera, R.; Vera, D.; Torreglosa, J.P. Integrated Multi-Criteria Decision-Making Approach for Power Generation Technology Selection in Sustainable Energy Systems. *Renew. Energy* **2025**, 243, 122481.
49. Sendek-Matysiak, E. A Multi-Criteria Evaluation of Powertrain Options for Long-Term Rental with Implications for Sustainable Transport. *Sustainability* **2026**, 18, 553.
50. Saaty, R.W. The Analytic Hierarchy Process—What It Is and How It Is Used. *Math. Model.* **1987**, 9, 161–176.
51. Hwang, C.L.; Yoon, K. Methods for Multiple Attribute Decision Making. In *Multiple Attribute Decision Making*; Springer: Berlin/Heidelberg, Germany, 1981.
52. Aiello, G.; Quaranta, S.; Inguanta, R.; Certa, A.; Venticinque, M. A Multi-Criteria Decision-Making Framework for Zero Emission Vehicle Fleet Renewal Considering Lifecycle and Scenario Uncertainty. *Energies* **2024**, 17, 1371.
53. Shayan, M.E.; Najafi, G.; Lorenzini, G. Optimization of a Dual Fuel Engine Based on Multi-Criteria Decision-Making Methods. *Therm. Sci. Eng. Prog.* **2023**, 44, 102055.
54. Sivaraja, C.M.; Sakthivel, G. Compression Ignition Engine Performance Modelling Using Hybrid MCDM Techniques for the Selection of Optimum Fish Oil Biodiesel Blend at Different Injection Timings. *Energy* **2017**, 139, 118–141.
55. Dornhof, J. Plug-In Hybrid Vehicle CO_2 Emissions: How They Are Affected by Ambient Conditions and Driver Mode Selection; Graz University of Technology: Graz, Austria, 2020.
56. Delkhosh, M.; Aliramezani, M.; Irannejada, M.; Lashgarian Azad, N. Optimal Control of Hybrid Electric Vehicles by Considering Engine and Tire/Road Noises. *Sci. Iran. Trans. B: Mech. Eng.* **2021**, 28, 3129–3140.
57. Archard, J.F. Contact and Rubbing of Flat Surfaces. *J. Appl. Phys.* **1953**, 24, 981–988.
58. Heywood, J.B. *Internal Combustion Engine Fundamentals*; McGraw-Hill: New York, NY, USA, 1988.
59. Miner, M.A. Cumulative Damage in Fatigue. *J. Appl. Mech.* **1945**, 12, A159–A164.
60. Stephens, R.I.; Fatemi, A.; Stephens, R.R.; Fuchs, H.O. *Metal Fatigue in Engineering*, 2nd ed.; Wiley: New York, NY, USA, 2000.
61. Dowling, N.E. Mechanical Behavior of Materials: Engineering Methods for Deformation, Fracture, and Fatigue, 4th ed.; Pearson: Boston, MA, USA, 2012.
62. Norton, M.P.; Karczub, D.G. *Fundamentals of Noise and Vibration Analysis for Engineers*, 2nd ed.; Cambridge University Press: Cambridge, UK, 2003.
63. Boix-Cots, D.; Ishizaka, A.; Fuente, A.; Pujadas, P. Beyond the Combustion Motor: A MCDM-Based Approach to Analyse the Alternative Fuel Vehicle Decision from the Customers' Point of View. *J. Clean. Prod.* **2025**, 486, 144564.

 doi:10.20944/preprints202604.2108.v1